Quasi-static fracture analysis by coupled three-dimensional peridynamics and high order one-dimensional finite elements based on local elasticity

Original
Quasi-static fracture analysis by coupled three-dimensional peridynamics and high order one-dimensional finite elements based on local elasticity / Pagani, A.; Enea, M.; Carrera, E.. - In: INTERNATIONAL JOURNAL FOR NUMERICAL METHODS IN ENGINEERING. - ISSN 0029-5981. - STAMPA. - 123:4(2022), pp. 1098-1113. [10.1002/nme.6890]

Publisher:
John Wiley and Sons Ltd

Published
DOI:10.1002/nme.6890

Received: 26 August 2021 | Revised: 2 November 2021 | Accepted: 5 November 2021

DOI: 10.1002/nme.6890

RESEARCH ARTICLE

WILEY

Quasi-static fracture analysis by coupled three-dimensional peridynamics and high order one-dimensional finite elements based on local elasticity

Alfonso Pagani | **Marco Enea** | **Erasmo Carrera**

Mul2 Research Group, Department of Mechanical and Aerospace Engineering, Politecnico di Torino, Torino, Italy

Correspondence
Alfonso Pagani, Mul2 Research Group, Department of Mechanical and Aerospace Engineering, Politecnico di Torino, Corso Duca degli Abruzzi 24, 10129 Torino, Italy.
Email: alfonso.pagani@polito.it

Funding information
H2020 European Research Council, Grant/Award Number: 850437; Ministero dell'Istruzione, dell'Università e della Ricerca, Grant/Award Number: 2017ZX9X4K

Abstract
This work investigates quasi-static crack propagation in specimens made of brittle materials by combining local and non-local elasticity models. The portion of the domain where the failure initiates and then propagates is modeled via three-dimensional bond-based peridynamics (PD). On the other hand, the remaining regions of the structure are analyzed with high order one-dimensional finite elements based on the Carrera unified formulation (CUF). The coupling between the two zones is realized by using Lagrange multipliers. Static solutions of different fracture problems are provided by a sequential linear analysis. The proposed approach is demonstrated to combine the advantages of the CUF-based classical continuum mechanics models and PD by providing, in an efficient manner, both the failure load and the shape of the crack pattern, even for three-dimensional problems.

KEYWORDS
fracture, high order finite elements, non-local elasticity, peridynamics

1 | INTRODUCTION

Over the last decades, several models have been proposed in order to better understand the complex mechanism of the failure process. In Reference 1, Griffith led the path toward the so-called linear elastic fracture mechanics (LEFM) by investigating the failure in glass through the principle of energy conservation. Williams[2] showed that, in the case of isotropic and elastic material, the stress field at crack tip tends to infinity, resulting in a mathematical singularity. For this reason, external criteria (such as critical energy release rate and stress intensity factor) are needed in order to capture crack initiation and growth in classical mechanics. The most used method for failure analysis has been the finite element method (FEM), a powerful tool for modeling complex structures and materials. Nevertheless, its governing equations are based on spatial derivatives of displacements, which are not defined at discontinuities, like a crack. Thus, external criteria are still needed for crack nucleation and for guiding the crack path, which is not autonomous.

A turning point for failure analysis via the FEM method is represented by the introduction of the cohesive zone element (CZE) by Hillerborg et al.[3] after the formulation of the concept by Dugdale[4] and Barenblatt.[5] This formulation allows to remove the singularity at the crack tip. A traction–separation law for describing the material behavior is employed. According to this formulation, when the crack opens, traction increases until the tensile strength is reached and then

---

reduces to zero. These elements are usually placed at elements boundaries, making the crack propagate only between regular elements. The shortcomings of CZEs are the dependency of the crack path to the mesh alignment, requiring an iterative remeshing when the crack path is not known. Cohesive elements have been employed in several applications, such as crack growth analysis in ductile materials,[6] impact damage in brittle materials,[7] and analysis of sandwich structures.[8]

This limitation has been overcome by the introduction of the concept of extended finite element method (XFEM) by Moes et al.,[9] which allows to model crack propagation without any remeshing. The fracture propagates on surfaces within a regular element. The only disadvantage remains that it still requires some external criteria in order to be able to solve fracture problems. Some examples of XFEM models for crack propagation are presented in References 10 and 11.

Non-local theories have also been introduced to overcome all the limitations of continuum mechanics when fracture problems are solved. According to these theories, a given property in a point of the domain depends on all the points which fall within a prescribed horizon. A recent non-local theory is peridynamics (PD). It has been formulated by Silling[12] in its seminal work. It represents an alternative to continuum mechanics. This theory assumes that a solid body is made of physical particles. Pairs of these particles develop an interaction only when their distance is lower than a fixed horizon radius δ. It is based on integro-differential equations, making this theory a powerful tool for describing discontinuous displacement fields, such as in fracture mechanics. Xu et al.[13] used PD for analysis of damage and failure in composite structures. Silling and Askari[14] developed a PD-based damage model for the investigation of crack nucleation and growth under cyclic loading. Ha and Bobaru[15,16] studied dynamic brittle fractures with PD. Madenci et al.[17] developed a method for the investigation of crack propagation in structures under complex loading conditions. Wang et al.[18] formulated a 3D conjugated bond-based PD where two materials particles are related through the rotation of the bond angles. This assumption allows to eliminate the constraining of Poisson's ratio value for bond-based PD.

The main disadvantage of PD theory is due to its non-local nature. In fact, methods used for solving this type of problem involve large, sparse, and not banded matrix, leading to high computational demand. Moreover, this aspect is amplified when dealing with 3D PD grids, where the number of interactions between particles can make the solution of most of the engineering problems prohibitive. For this reason, researchers are working on coupling FEM model based on classical elasticity and PD regions in order to exploit the advantages of both methodologies. Several techniques have been proposed in the recent years. In Reference 19, a local–nonlocal coupling is achieved by connecting subregions with constant horizon through the introduction of the partial stress concept. This method, where interaction forces between nodes and particles are transferred, has been further developed in References 20 and 21. In Reference 22, a morphing strategy based on energy equivalence is adopted. Seleson and his co-authors proposed a force-based blended model for coupling of PD and classical elasticity. Kilic and Madenci[23] introduced an overlapping region where both the FEM and the PD equations are valid at the same time. In Reference 24, Oterkus proposed a global-local approach, where the global model is created via FEM model, while the PD theory is employed for local modeling in order to perform failure analysis. Sun and Fish[25] introduced a superposition-based coupling model between bond-based PD and FEM. A partial superposition of nonlocal (PD) and local (FEM) solution is considered. The continuity of the solution is achieved by imposing appropriate homogeneous boundary conditions. The authors extended this method to the coupling of non-ordinary state-based PD and FEM in Reference 26.

Note that most of the coupling methods in the literature involve dimensionally consistent domains: 1D FEM with 1D PD grid, 2D with 2D, and 3D with 3D. The work by Pagani and Carrera[27] proposed a coupling method between refined 1D FEs and 3D PD grids, based on Lagrange multipliers. This model allowed to deal with complex 3D problems while reducing the computational cost of the analysis. The method was validated for linear static analysis by comparing the results with full FEM models.

The present work aims at employing this method to deal with progressive failure analysis in brittle materials. The possibility of bond breakage is introduced in the proposed method. The so-called "bond stretch criterion" is used for failure investigation; the bond between two connected particles is broken if subjected to a stretch greater than a critical value. Sequentially linear analysis is performed on pre-cracked structures, as proposed in Reference 28. According to the comparison between stretch and critical value for each bond, bonds conditions are updated at each iteration. The removal of a bond causes a reduction in stiffness of the interested zone, leading to a possible crack propagation zone that will be unguided and autonomous, differently from most of the continuum mechanics models.

The article is organized as follows: Section 2 introduces bond-based PD theory and the discretized equations; then, high-order 1D FEs in the CUF framework and the coupling with PD sub-domains are discussed in Section 3; the failure algorithm proposed in this article is detailed in Section 4; next, two representative numerical results are presented in Section 5; finally, Section 6 summarizes important conclusions.

2 | BOND-BASED PD

2.1 | Linear static equilibrium equation

In PD, two particles $\boldsymbol{x}$ and $\boldsymbol{x}'$ have a direct physical interaction when their distance is lower than a prescribed horizon radius, indicated with δ. A schematic representation of some significant parameters in PD theory is shown in Figure 1.

The relative position of these two particles is denoted by the vector ξ:

$$\xi = \boldsymbol{x}' - \boldsymbol{x}, \tag{1}$$

whereas the relative displacement vector is indicated by $\boldsymbol{\eta}$:

$$\boldsymbol{\eta} = \boldsymbol{u}' - \boldsymbol{u}. \tag{2}$$

In Equation (2), $\boldsymbol{u}$ and $\boldsymbol{u}'$ are the displacement of particle $\boldsymbol{x}$ and $\boldsymbol{x}'$, respectively. It can be easily noted that the quantity $\boldsymbol{\eta} + \xi$ is the relative position vector of two particles at a specific instant of time. The direct interaction between two particles is called a *bond*, which extends over a finite distance. The particle $\boldsymbol{x}'$ exerts a force $\boldsymbol{T}(\boldsymbol{\eta}, \xi)$ on particle $\boldsymbol{x}$. $\boldsymbol{T}$ is a pairwise force (per unit volume squared) function. It is symmetric, and disappears for $|\xi| > \delta$. If two particles have a distance shorter than this radius, they will exert the pairwise force $\boldsymbol{T}$ on each other. On the contrary, if their distance is greater than δ, the particles does not have any kind of interaction.

Silling[12] introduced the static equilibrium equation of a particle $\boldsymbol{x}$. It takes the following integral form:

$$\int_{\mathcal{H}_x} \boldsymbol{T}(\boldsymbol{\eta}, \xi)\, \mathrm{d}V'_x + \boldsymbol{b}(\boldsymbol{x}) = \boldsymbol{0}, \tag{3}$$

where $\mathcal{H}_x$ is a neighborhood of $\boldsymbol{x}$ and $\boldsymbol{b}$ is a body force density field. The assumption that the bond force $\boldsymbol{T}$ depends only on the bond stretch is made. This quantity is defined by the scalar s, which has the following form:

$$s = \frac{|\boldsymbol{\eta} + \xi| - |\xi|}{|\xi|}. \tag{4}$$

The stretch s and the pairwise force function $\boldsymbol{T}$ are related by:[12]

$$\boldsymbol{T} = c\, s\, \frac{\boldsymbol{\eta} + \xi}{|\boldsymbol{\eta} + \xi|} \cong c\, s\, \frac{\xi}{|\xi|}, \tag{5}$$

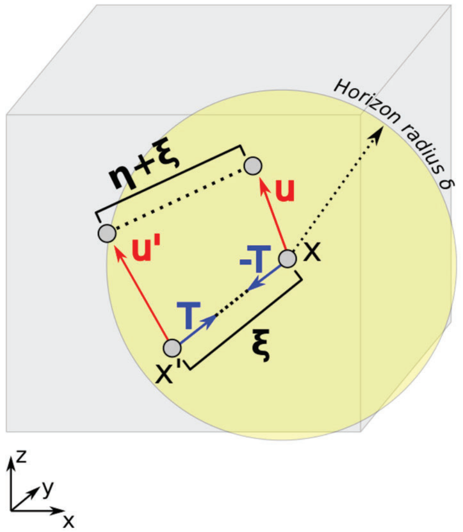

FIGURE 1 Graphic representation of significant parameters in the peridynamic theory. Particles $\boldsymbol{x}$ and $\boldsymbol{x}'$ have a relative distance ξ, lower than a prescribed horizon radius δ. These particle will exchange a pairwise force $\boldsymbol{T}(\xi, \boldsymbol{\eta})$, where $\boldsymbol{\eta}$ is the relative displacement

where c is the bond stiffness and $\boldsymbol{n} = \frac{\eta+\xi}{|\eta+\xi|}$ the stretch direction. It has been simplified as $\frac{\xi}{|\xi|}$ under the assumption of small displacements. The bond stiffness c can be written as function of Young modulus E and horizon radius δ. In the case of 3D bodies, one has[29]

$$c = \frac{12E}{\pi\delta^4}. \tag{6}$$

Nevertheless, the assumptions made lead to a limitation of the Poisson ratio. In fact, in case of 3D bond-based PD, its value is constrained to $\nu = 0.25$. This limitation has been removed in the state-based PD, a more general formulation introduced by Silling et al.[30]

2.2 | Discretization

The PD region is discretized into nodes, arranged into a grid. Each node has a known volume in the reference configuration. After discretization, the static equilibrium integral equation (Equation 3) of the node $\boldsymbol{x}_i$ is written as a summation:

$$\sum_{j=1}^{N_{\mathcal{H}_i}} \boldsymbol{T}_{ij}\ V_j + \boldsymbol{b}_i = 0, \tag{7}$$

where $N_{\mathcal{H}_i}$ is the number of family nodes of $\boldsymbol{x}_i$ and V_j is the volume of particle $\boldsymbol{x}_j$. In the proposed work, $V_j = \Delta x^3$, where Δx is the grid spacing, assumed to be constant in all three directions. Moreover, in order to take into account the reduction in volume of a particle that does not entirely lay within the horizon radius (as in the case of particle x_r in Figure 2), the volume reduction scheme proposed in Reference 31 is employed.

After linearization (Equation 5), and considering only homogeneous media, Equation (7) becomes:

$$\sum_{j=1}^{N_{\mathcal{H}_i}} \boldsymbol{C}(\boldsymbol{x}_j - \boldsymbol{x}_i)\ (\boldsymbol{u}_j - \boldsymbol{u}_i)\ V_j + \boldsymbol{b}_i = 0, \tag{8}$$

where $\boldsymbol{C}$ is the material's *micromodulus function*, whose value is a second-order tensor.

It can be observed that by multiplying Equation (8) to V_i, an equilibrium equation formally equal to the one of finite element analysis is obtained.[32]

$$\sum_{j=1}^{N_{\mathcal{H}_i}} \boldsymbol{C}(\boldsymbol{x}_j - \boldsymbol{x}_i)\ (\boldsymbol{u}_j - \boldsymbol{u}_i)\ V_i V_j + \boldsymbol{b}_i V_i = 0 \tag{9}$$

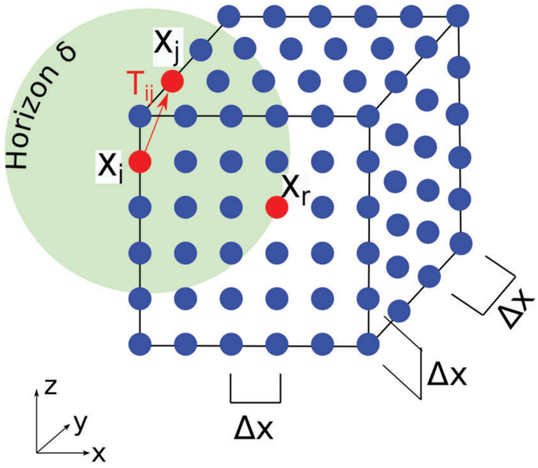

FIGURE 2 Discretization of a 3D PD region. Grid spacing Δx is constant along all three directions. Each node has a volume $V = \Delta x^3$. The particle x_i exerts a force T_{ij} on the particle x_j. x_r is an example of particle which does not entirely lay within the horizon radius δ

or

$$\boldsymbol{K}^{\mathrm{PD}}\boldsymbol{U}^{\mathrm{PD}} = \boldsymbol{F}^{\mathrm{PD}}. \tag{10}$$

3 | HIGH ORDER 1D FINITE ELEMENTS

In the proposed work, 3D PD grids are coupled with 1D FEs, based on the Carrera unified formulation (CUF). It is a methodology capable of generating high-order theories with great accuracy and a significant reduction of the computational demand.[33]

3.1 | The Carrera unified formulation

Consider a generic beam structure aligned along the y axis, with length equal to l. The cross-section Ω is normal to the beam axis y. The validity of the formulation does not depend on the cross-section shape. In the CUF's framework, the 3D displacement field of such a beam is written in the following form:

$$\mathbf{u}(x, y, z) = F_\tau(x, z)\mathbf{u}_\tau(y), \quad \tau = 1, 2, \dots, M, \tag{11}$$

where $\mathbf{u}(x, y, z)$ is the displacement vector; F_τ are the cross-section expansion functions; $\mathbf{u}_\tau$ is the generalized displacement vector; M is the number of terms in the expansion. The subscript τ indicates summation. Additionally, F_τ and M can be chosen arbitrarily. The choice of these expansion functions establishes the class of the one-dimensional CUF model. This choice is related to the required degree of accuracy and the problem's features to solve. In the framework of CUF, Taylor expansion (TE) models have been widely used, as in References 34 and 35. In the case of TE models, the generalized displacements are expanded around the beam axis through Mclaurin polynomials of truncated order N. The order N is arbitrary and determines the beam theory. TE models are very efficient for various problems, but some inaccuracies are introduced when dealing with short beams or complex structures. In order to solve these types of problems, Lagrange expansion (LE) models are employed. In this case, the generalized displacements are expanded around the beam axis through Lagrange-like polynomials. The cross-section surface can be discretized into different expansion sub-domains. The polynomial degree of each one of these sub-domain depends on which Lagrange expansion model is employed. In Reference 36, various Lagrange polynomials have been introduced, such as three-point linear (L3), four-point bi-linear (L4), and nine-point bi-quadratic (L9) polynomials. The main feature of LE models is that they make use of local expansions of pure displacement variables. The most important advantage is that it allows a finer discretization in particular zones of interest, leading to a higher solution accuracy. Moreover, it enables to capture 3D-like solutions at a global-local scale.

3.2 | Finite element approximation and coupling with PD sub-domains

The generalized displacement introduced in Equation (11) can be approximated along the beam axis via discretization with 1D finite elements (FEs):

$$\boldsymbol{u}_\tau(y) = N_i(y)\, \boldsymbol{u}_{\tau i}, \quad i = 1, 2, \dots, N_n + 1, \tag{12}$$

where N_n is the number of nodes for each element. In Equation (12), i indicates summation. The generalized displacements are written as a function of the unknown nodal vector, $\boldsymbol{u}_{\tau i}$, and the standard 1D shape functions, N_i. It should be noted that Equation (12) is valid independently of the refined 1D theory that is adopted. The use of a compact notation allows a unified and hierarchical formulation of the governing equations and matrices.

The governing equations are written using the principle of virtual work. For example, in the case of linear elastic, static problems, it reads:

$$\delta L_{\mathrm{int}} = \delta L_{\mathrm{ext}}, \tag{13}$$

where δ indicates the virtual variation, L_{int} the work of the internal strain energy, and L_{ext} the work of the external forces. The internal work takes the following expression:

$$\delta L_{\text{int}} = \int_l \int_\Omega \delta \boldsymbol{\epsilon}^T \boldsymbol{\sigma} \, \mathrm{d}\Omega \, \mathrm{d}y, \tag{14}$$

where $\boldsymbol{\sigma}$ and $\boldsymbol{\epsilon}$ are the vectors of 3D stresses and strains. By replacing the constitutive and geometric equations along with Equations (11) and (12), the expression of the internal work is rewritten in the following compact form:

$$\delta L_{\text{int}} = \delta \boldsymbol{u}_{sj}^T \mathbf{K}^{\tau sij} \mathbf{u}_{\tau i}, \tag{15}$$

where $\mathbf{K}^{\tau sij}$ is the 3×3 fundamental nucleus of the element stiffness matrix of the arbitrarily refined 1D beam theory. The derivation of the FE fundamental nucleus of the stiffness matrix can be found in Reference 33. The expansion of the fundamental nucleus within the stiffness matrix on the four indexes τ, s, i, and j allows to formulate any refined beam model automatically. Hence, after expansion of the stiffness matrix according to the approximation order and after assembly over the whole domain, Equation (13) is compacted in the following expression:

$$\boldsymbol{K}^{\text{FE}} \boldsymbol{U}^{\text{FE}} = \boldsymbol{F}^{\text{FE}}, \tag{16}$$

where $\boldsymbol{U}^{\text{FE}}$ is the vector of the FE nodal unknowns and $\boldsymbol{F}^{\text{FE}}$ is the vector of external forces.

Let now consider a solid beam in a Cartesian reference system, as in Figure 3. The central portion of the beam is modeled via 3D PD, while the remaining domains are discretized through higher-order 1D FEs.

Given an interface (contact) zone $\mathcal{I}$ between the peridynamic region and the 1D finite elements, Lagrange multipliers are employed to fulfill the congruence conditions on $\mathcal{I}$. Consider a single peridynamic particle k of the contact region $\mathcal{I}$. The system to be solved is completed by adding the Lagrangian of each particle k.

After the Lagrangian of each particle $k \in \mathcal{I}$ is found, the linear system in matrix form is written in the following way:

$$\begin{bmatrix} \boldsymbol{K} & \boldsymbol{B}^T \\ \boldsymbol{B} & \mathbf{0} \end{bmatrix} \begin{Bmatrix} \boldsymbol{U} \\ \lambda \end{Bmatrix} = \begin{Bmatrix} \boldsymbol{F} \\ \mathbf{0} \end{Bmatrix}, \tag{17}$$

where $\boldsymbol{B}$ is the coupling matrix and $\boldsymbol{K}$ is the global stiffness matrix. The unknowns of the problem are the vectors $\boldsymbol{U}$ and λ (Lagrange multipliers' vector). The computation of these quantities leads to the solution of the coupled problem.

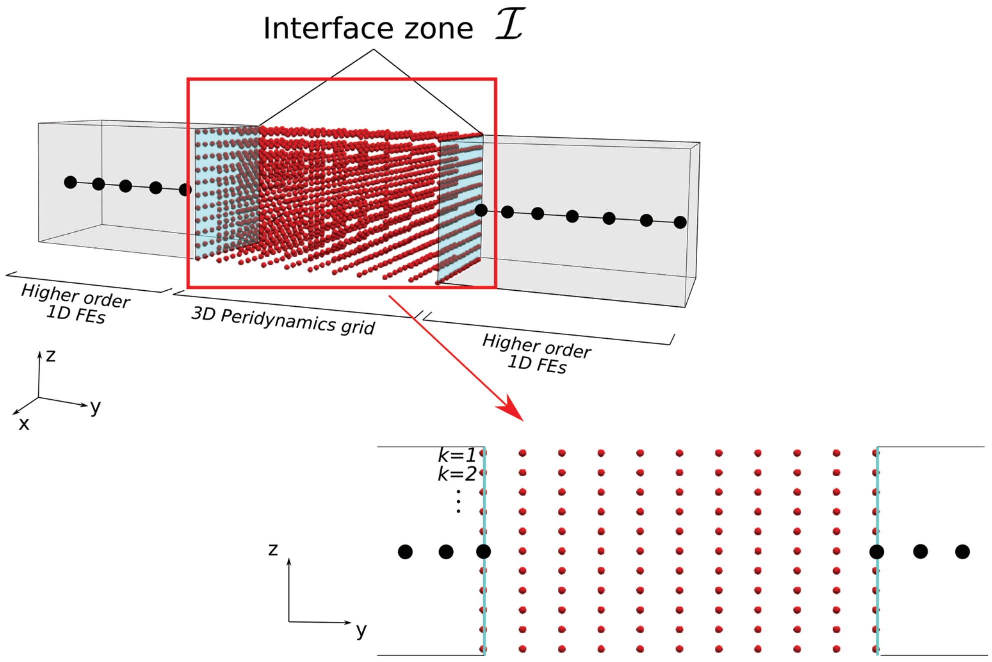

FIGURE 3 Refined 1D finite elements are coupled with PD particles through Lagrange multipliers. The Lagrangian of each particle k at the interface zone $\mathcal{I}$ is added to the system in order to satisfy displacement continuity

For further information about the proposed coupling model, interested readers can refer to Reference 27. This method is valid for 1D finite elements of any order. Furthermore, this methodology has proven to be very effective for coupling 1D high order FEs and 3D PD. In fact, it allowed to reproduce results with a 3D accuracy while sensibly reducing the computational cost compared to a full three-dimensional peridynamic analysis. Thus, the PD domain could be employed only in regions of the structure where they could be more appropriate, such as in zones where a crack is likely to develop.

4 | FAILURE MODEL

In a PD framework, material damage can be directly introduced in the constitutive model by allowing the bonds between particles to break. In the case of bond-based PD, the most used failure criteria is the bond stretch criterion, introduced by Silling and Askari.[37] According to this criterion, a bond is considered broken when it undergoes a stretch greater than its critical value s_c. When it occurs, the pairwise force between the involved points is irreversibly removed. As a result, the load will be distributed on all the other bonds, leading to unguided crack initiation.

In order to set to zero the pairwise force between two points, a history-dependent scalar function μ has to be introduced:

$$\mu(\boldsymbol{\eta}, \boldsymbol{\xi}) = \begin{cases} 1, & s < s_c, \\ 0, & s \geq s_c. \end{cases} \tag{18}$$

A different scalar μ is created for each pair of particles within the horizon radius δ. This scalar is then introduced into Equation (5), that will be modified as follows:

$$\boldsymbol{T}(\boldsymbol{\eta}, \boldsymbol{\xi}) = \mu(\boldsymbol{\eta}, \boldsymbol{\xi}) cs\boldsymbol{n}. \tag{19}$$

Thus, when the critical stretch between two particles is reached, the corresponding scalar function μ will be equal to 0, and the pairwise force $\boldsymbol{T}$ will be removed.

The critical stretch is assumed to be constant in all the material. Its value has been computed through energetic considerations in Reference 37. Specifically, the critical stretch value is obtained by equating the energy required for breaking all the bonds that previously connected two halves of a fracture surface with the critical energy release rate G_0. Under the assumption of LEFM for an isotropic material and a 3D PD grid, the critical stretch value s_c is:

$$s_c = \sqrt{\frac{5G_0}{6E\delta}}. \tag{20}$$

The advantage of introducing failure directly at a bond level is the possibility of a unique identification of local damage, defined by the scalar function φ_x

$$\varphi_x = 1 - \frac{\int_{H_x} \mu(\boldsymbol{\eta}, \boldsymbol{\xi}) dV_{x'}}{\int_{H_x} dV_{x'}} \tag{21}$$

called *damage index*. The subscript x indicates that the damage index is a property of the single-particle x. The function φ_x can take all values from 0 to 1. A value of 0 represents an intact bond, while a value of 1 indicates that all the bonds involving the source point are broken. Thus, the point is disconnected from the structure. In Figure 4, an example of φ_x calculation for a single particle x (in red in the figure) is shown. The assumption made is that a crack is created when a value of $\varphi_x \geq 0.5$ is reached.

In this work, sequentially quasi-static linear analyses are performed. An increasing displacement is applied at each step. After solving the linear problem, the value of the bond stretch s is computed for each pair (i, j) of particles within the horizon radius δ. Then, this stretch is compared with the critical bond stretch s_c, calculated through Equation (20). If $s(i, j)$ is greater than s_c for one or more bonds, then the pairwise force exchanged between the involved points will be removed by setting the value of the scalar $\mu(i, j)$ to 0. Finally, the value of the damage index φ_x for each particle x is computed in order to have a graphic visualization of crack initiation and propagation. If any bond has been broken, they will be removed in the following iteration. Figure 5 shows a flowchart representing the entire algorithm, introduced by Ni et al.[28]

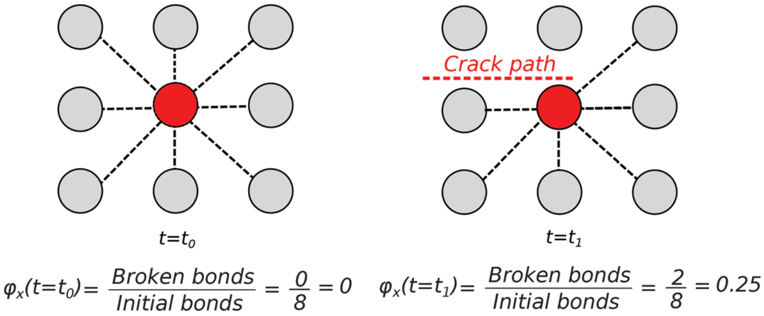

FIGURE 4 Example of computation of the damage index φ for a single point (in red). Only the interactions involving this point are represented for the sake of clarity

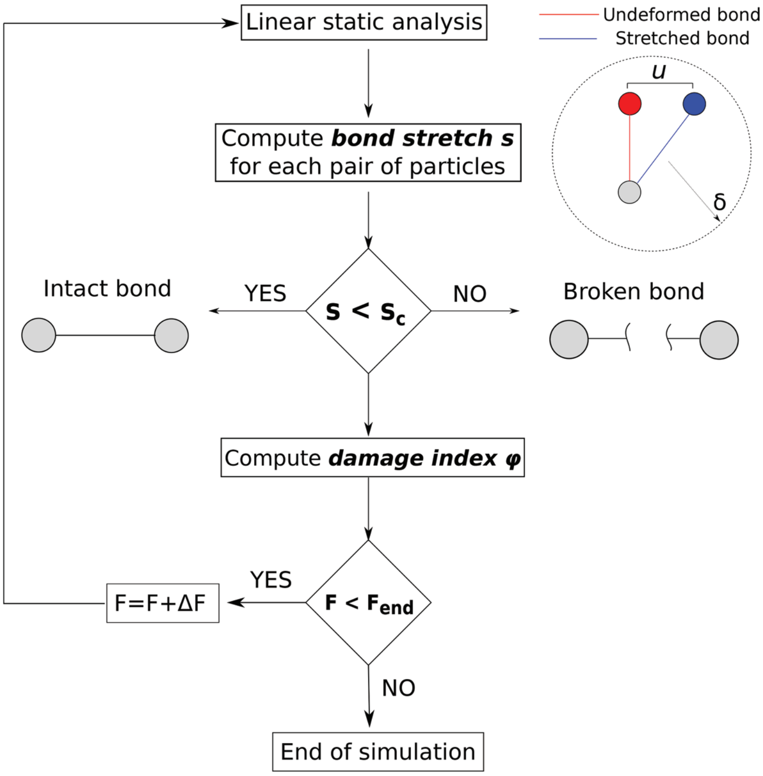

FIGURE 5 Flowchart representing the failure algorithm for the proposed coupled model

5 | NUMERICAL RESULTS

5.1 | Bar under uniaxial tension

The first case study is a bar under uniaxial tension. It has already been studied in Reference 38. The geometry is shown in Figure 6. The bar is 200 mm long and has a rectangular cross-section with sides equal to 40 and 100 mm. Two steel plates of 5 mm are present at both ends in order to apply loads and boundary conditions. A crack is introduced at the center of the bar, with a crack width of 4 mm. The plate at $y = 0$ is clamped, while the end plate is subjected to an axial displacement. The bar is made of a homogeneous isotropic material with Young modulus $E = 32$ GPa. The Poisson's coefficient is $\nu = 0.25$ in the peridynamic domain. The value of the critical energy release rate G_0 is 60 N/m^2.

The PD grid is located in the central zone of the bar, from the coordinate $y = 60$ mm to $y = 140$ mm. The remaining zones are modeled via finite elements. The discretization along the longitudinal axis consists of four two-node linear finite elements (B2), two for the steel plates and two for the bar. The cross-section is discretized with a single L9 element. This

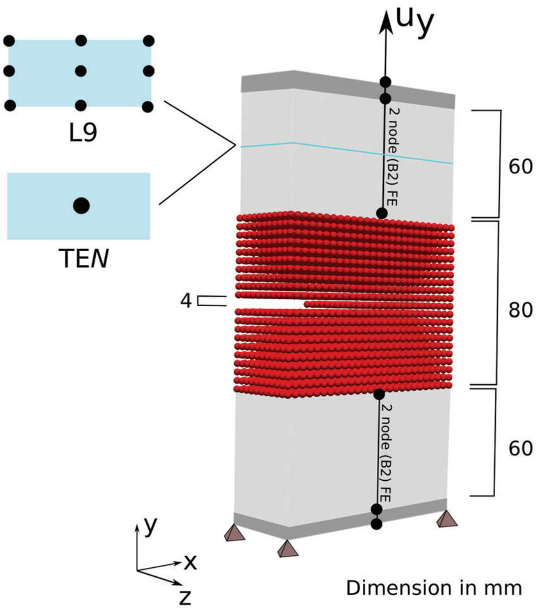

FIGURE 6 Geometry and boundary conditions of the investigated traction bar

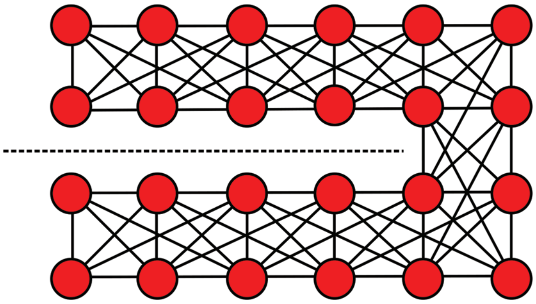

FIGURE 7 Graphic representation of the crack opening through removal of involved bonds

discretization has been chosen because it demonstrated to be the most accurate for a similar traction problem, investigated in Reference 27. Nevertheless, TE models are also employed in order to study the influence of the 1D theory on the model's accuracy.

In the reference study, the progressive failure in the structure is investigated through cohesive and bulk elements. In this work, the assumption that the crack starts and propagates only in the PD domain is made. In Figure 6, a crack was simulated through the removal of PD nodes, just for explicative reasons. In fact, in the present model, a crack is created by removing bonds between the two edges of the open surface, as shown in Figure 7. Thus, the involved particles will have a lower number of initial bonds than the neighboring ones, resulting in lower stiffness and a plausible crack initiation zone.

As previously mentioned in Section 4, sequentially linear analysis have been performed while increasing the applied displacement and updating the scalar functions μ according to the bond stretch criterion. The evolution of the crack pattern is shown in Figure 8. Damage index φ for each particle at four different steps of the simulation are displayed. In this case, its evolution indicates that the crack propagates in a direction parallel to the pre-existing crack, in accordance with experimental tests and numerical simulations.

In Figure 9A, the curves of crack mouth opening displacement (CMOD) versus forces for different cases are shown. The *numerical reference* curve is provided by Durand and Silva,[38] where the authors implemented a model that includes cohesive elements and plasticity. The other curves have been obtained via the FEM-PD coupling method proposed in this work. The influence of the grid spacing Δx and the horizon radius δ on CMOD and peak load has been investigated. These curves are shown in Figure 9A. The numerical values for peak loads and corresponding CMODs are summarized in Table 1.

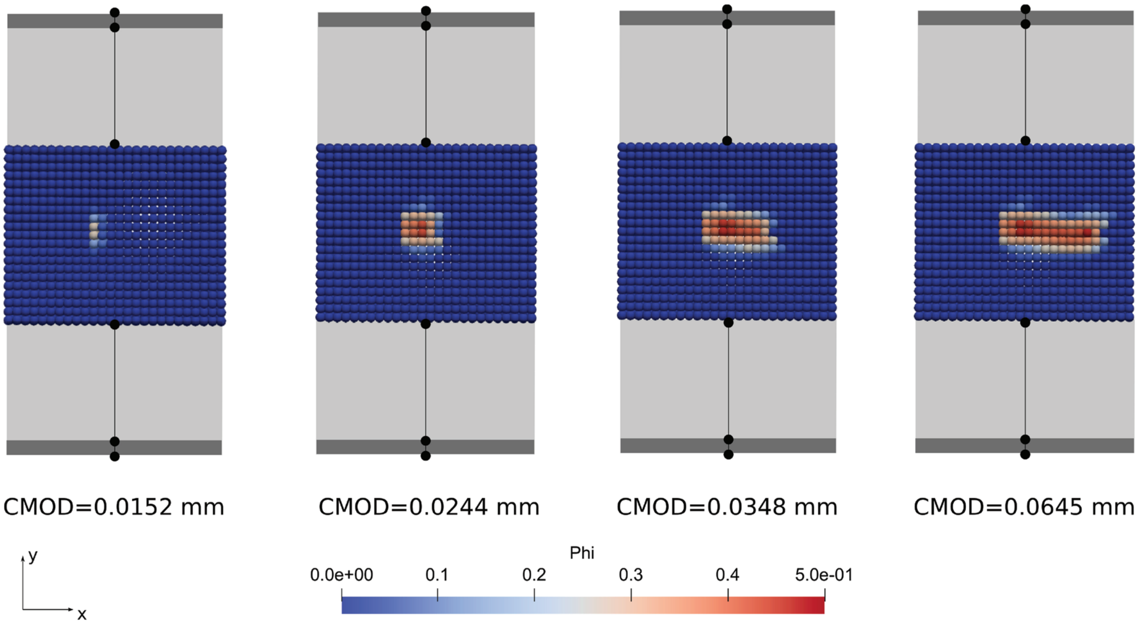

FIGURE 8 Evolution of the distribution of the damage index φ, which gives information about the crack propagation

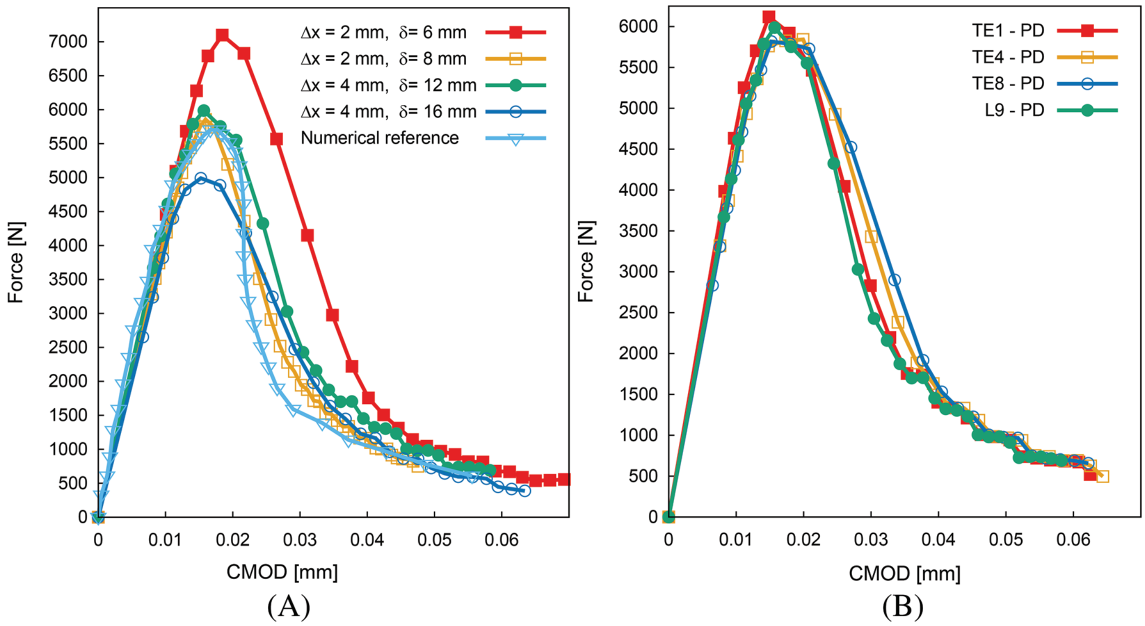

FIGURE 9 CMOD–force curves: (A) Effect of grid spacing Δx and horizon radius δ on the present L9-PD model and comparison with numerical results.[38] (B) Effect of different 1D-CUF models for FEM regions, with fixed grid spacing ($\Delta x = 4$ mm) and horizon radius ($\delta = 12$ mm)

The first consideration is that there is a strong dependency of the peak load on the PD parameters. When comparing two simulations with fixed grid spacing Δx, but modifying the horizon radius, a not negligible variation of the failure load value arises. At the same time, the CMOD calculated at this stage presents very small discrepancies. More specifically, increasing δ leads to a reduction of the peak load. More in-depth convergence analysis (such as those introduced in Reference 39) is not performed, being out of the scope of this work.

The curves which are closest to the numerical reference are the simulation with $\Delta x = 2$ mm and $\delta = 4\Delta x = 8$ mm and the one with $\Delta x = 4$ mm and $\delta = 3\Delta x = 12$ mm. Both values of failure load and CMOD of these two curves are

TABLE 1 Summary of key parameters for both reference and simulation cases with different grid spacing Δx and horizon radius δ

Case	Δx (mm)	Horizon δ (mm)	FEM DOFs	PD DOFs	Peak load (N)	CMOD (mm)
Numerical reference	–	–	30,672	–	5700	0.017
L9-3D PD	2	6	162	131,733	7191	0.0193
L9-3D PD	2	8	162	131,733	5544	0.014
L9-3D PD	4	12	162	18,018	5986	0.0156
L9-3D PD	4	16	162	18,018	5020	0.015

TABLE 2 Summary of key parameters for simulation cases with different 1D-CUF models for FEM regions

			Peak load		CMOD	
Case	FEM DOFs	PD DOFs	Value (N)	Diff (%)	Value (mm)	Diff (%)
TE1-3D PD	54	18,018	6176	3.1	0.0152	−2.5
TE4-3D PD	270	18,018	5981	0.0	0.0161	3.2
TE8-3D PD	648	18,018	5980	0.0	0.0162	3.8
L9-3D PD	162	18,018	5986	–	0.0156	–

Note: Percentage difference of TE models respect to the L9-PD model is also shown.

comparable. Nevertheless, there is a difference of almost a magnitude order (18k vs. 131k) in the number of PD degrees of freedom (DOFs). Thus, reducing the grid spacing by a factor of 2 led to an abrupt increase in DOFs' number. This difference is practical proof that a full 3D peridynamic domain could easily reach an impracticable number of DOFs, which would make the problem too expensive to be solved.

Another interesting consideration could be made considering the theory and relative order employed to discretize the FEM region. In Figure 9B, the CMOD–force curves for different FEM discretization are shown. The grid spacing Δx and the horizon radius δ are fixed, with a value of 4 and 12 mm, respectively. In Table 2, some important parameters of the simulation are shown. In particular, the failure load and the corresponding CMOD are indicated for each case. The relative difference with the reference value of the L9-PD simulation is also shown. Note that these differences are negligible, from a maximum of 3.8% for the CMOD value to a practical zero-difference for the failure load. These analyses show that the solution is not affected by the theory of the FE model employed. This conclusion was already proven in Reference 27, where simple linear static analysis were performed.

5.2 | Brokenshire test

The second case study is the so-called Brokenshire test. It has been performed for the first time by Brokenshire.[40] The whole setup of the test is shown in Figure 10. A notched beam is considered, clamped at its extremities by two steel frames. Three loading arms of these frames are supported, while the remaining one is loaded with a vertical force or displacement. These boundary conditions induce a torsion on the notched beam. This problem is not symmetric as the previous one due to these boundary conditions and to the pre-existing crack pattern (45° angle). Thus, the high tri-dimensionality of the problem makes it a critical test for the coupled model proposed in this work.

The bar is 400 mm long, and it has a square cross-section with side length equal to 100 mm, while the steel plates have a length of 25 mm. The bar is made of a homogeneous isotropic material with Young modulus $E = 35$ GPa. The Poisson's coefficient is $\nu = 0.25$ in the peridynamic domain. The value of the critical energy release rate G_0 is 80 N/m^2. The PD grid is located in the central zone of the bar, from the coordinate $y = 125$ mm to $y = 325$ mm. The remaining zones are modeled via finite elements. The discretization along the longitudinal axis consists of two three-node quadratic (B3) elements (one for each steel plate) and a total of four four-node cubic (B4) elements for the bar. The cross-section is discretized with six L9 elements. More refined elements than the traction bar are used for both axial and cross-section discretization. The objective is an accurate description of the more complex torsional behavior.

As for the previous case, bonds between particles at the edge of the open crack are removed.

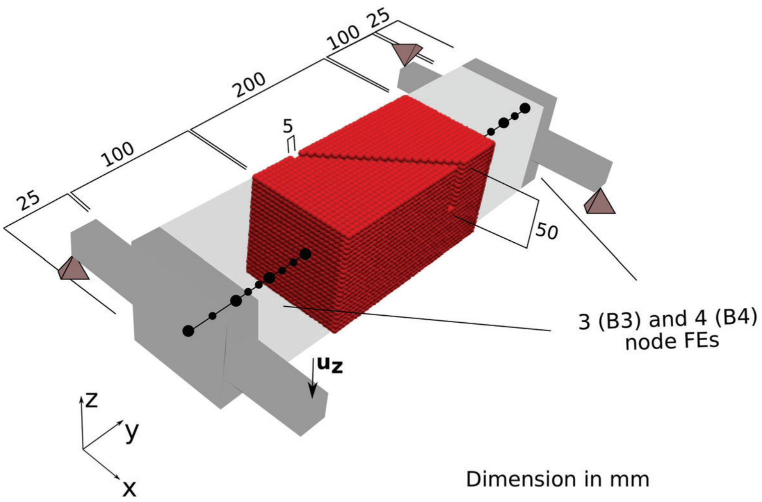

FIGURE 10 Geometry and boundary conditions of the bar investigated in a Brokenshire test

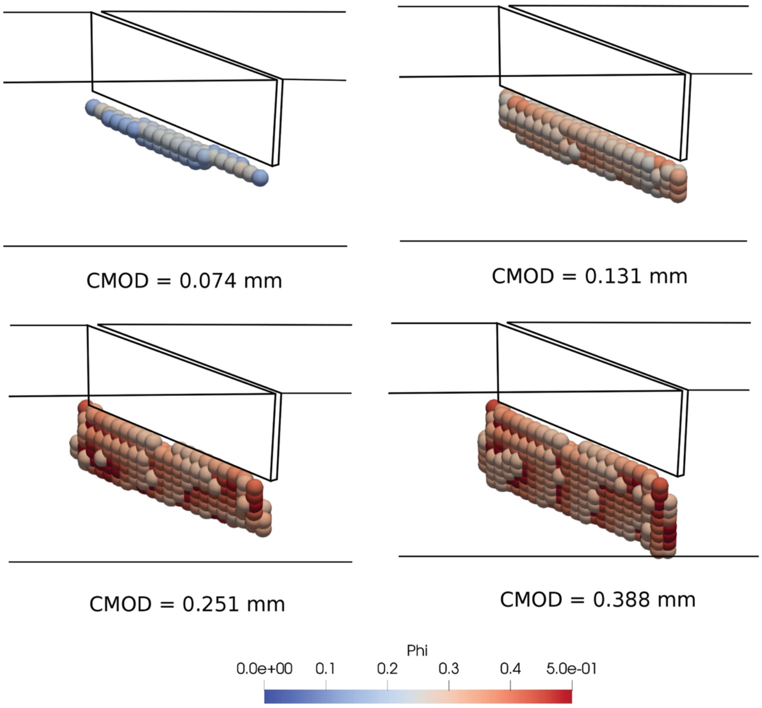

FIGURE 11 Evolution of the distribution of the damage index φ, which gives information about the crack propagation. For the sake of clarity, only the damaged particles are shown

Sequential linear analysis is then performed. In Figure 11, the value of the damage index φ for most interesting particles at four steps of the simulation are shown. The distribution of φ gives information about the propagation of the crack. The resultant front of the crack is in good accordance with both the experimental results[41] and the numerical simulations.[38,42-44]

In Figure 12, the comparison of the damage distribution between a plasticity-damage model[44] and the current model is shown. The crack pattern seen from the bottom of the beam is well reproduced.

For a better understanding of the crack propagation in the Brokenshire test, Figure 13 shows the deformed structure at the end of the simulation.

In Figure 14, the CMOD–force curves for different values of δ are shown, while the grid spacing Δx is equal to 5 mm. The CMOD is computed between two points at the center of the crack. The two other curves represent the experimental

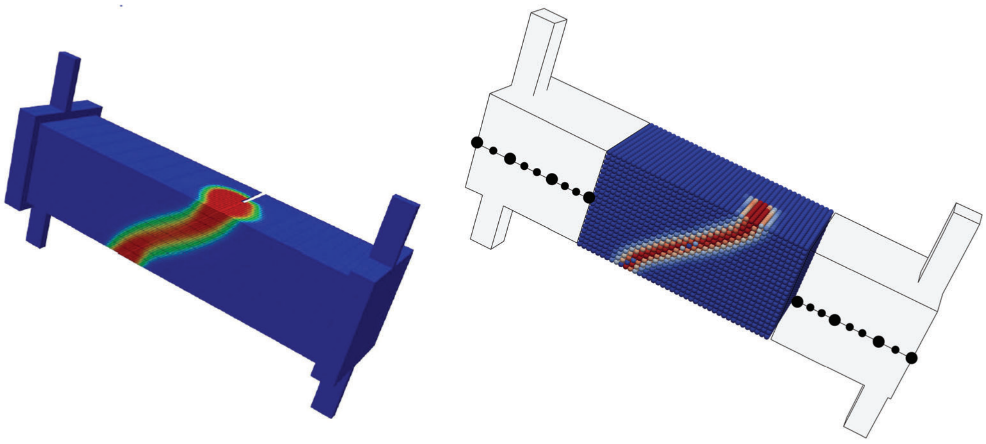

FIGURE 12 Damage index distribution from a plasticity-damage model (left, adapted from Reference 44) and the present model (right)

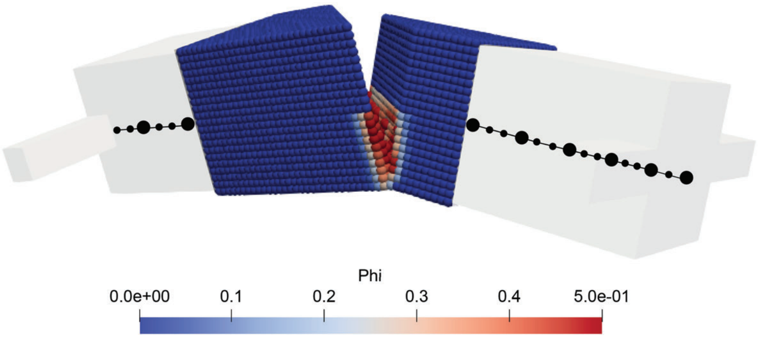

FIGURE 13 Distribution of the damage index ϕ at the end of simulation in the deformed configuration

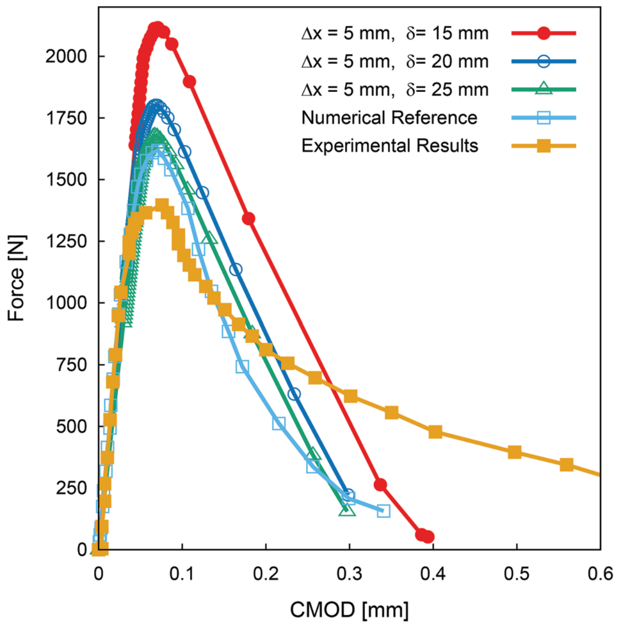

FIGURE 14 CMOD–force curves for different values of horizon radius δ for the Brokenshire test

TABLE 3 Summary of key parameters for both reference and simulation cases

Case	Δx (mm)	Horizon δ (mm)	FEM DOFs	PD DOFs	Peak load (N)	CMOD (mm)
Experimental results	–	–	–	–	1397	0.0075
Numerical reference	2.5	7.5	–	939,366	1618	0.007
1D FEM-3D PD	5	15	774	54,243	2117	0.0069
1D FEM-3D PD	5	20	774	54,243	1801	0.0067
1D FEM-3D PD	5	25	774	54,243	1678	0.0069

results[41] and a numerical reference,[45] respectively. The latter proposed a FEM-PD coupled model, where FEM nodes can be converted into PD nodes in order to follow the crack. Thus, for this particular case the number of PD DOFs in Table 3 indicates the total number of DOFs. A strong influence of the horizon radius on the peak load is witnessed in this structure. As in the previous case, an increase in the horizon radius δ results in a reduction of the failure load, while the corresponding CMOD is unchanged. The simulation with $\delta = 5\Delta x$ retrieves a value of failure load similar to the value found in the numerical reference, where a higher number of DOFs and a more complex model were employed. Nevertheless, a not negligible difference with the experimental failure load is still present.

As in the numerical reference results, the post-peak curve shows a nonlinear trend which is challenging to reproduce. In fact, it should be reminded that in the current model, quasi-static linear analysis are performed. In future work, the present model will be further enhanced to correctly replicate these nonlinearities.

6 | CONCLUSIONS

This work has proposed an implementation of a failure algorithm in an existing PD-FEM coupled model. This coupling has been realized between three-dimensional PD grids and higher-order one-dimensional finite elements through the well-known CUF. This method has proven to have a very high accuracy along with a significant reduction of the computational cost,[27] allowing to deal with complex and representative problems. The failure algorithm introduced in the model is based on the so-called "bond stretch criterion."[37] First, a pre-cracked bar under traction has been investigated. The crack pattern found by the model is in good accordance with both experimental and numerical simulations. Additionally, the force-CMOD curves as a function of two PD parameters (grid spacing Δx and horizon δ) are drawn. Both failure load and the relative CMOD correspond to the values found by the numerical simulation in Reference 38, where cohesive elements and plasticity were used.

The second case study was the well-known Brokenshire test.[40] A bar with a 45° crack at its center is subjected to torsion. It represents a highly three-dimensional problem. Even in this case, the proposed model is able to follow the propagation crack witnessed in the experimental test. The force-CMOD curve is well reproduced up to the peak load, while a not negligible error appears in the post-peak curve.

Future work will deal with the implementation of the more general state-based PD, which allows to eliminate all constraints on the Poisson ratio. Additionally, the current model will be enhanced in order to better describe the nonlinear behavior of the post-peak CMOD–force curves.

ACKNOWLEDGMENTS

This project has received funding from the European Research Council (ERC) under the European Union's Horizon 2020 Research and Innovation Programme (Grant Agreement No. 850437) and from the Ministero dell'Istruzione, dell'Università e della Ricerca, Research Funding Programme PRIN 2017 (2017ZX9X4K).

DATA AVAILABILITY STATEMENT

The data that support the findings of this study are available from the corresponding author upon reasonable request.

ORCID

Alfonso Pagani https://orcid.org/0000-0001-9074-2558
Erasmo Carrera https://orcid.org/0000-0002-6911-7763

REFERENCES

1. Griffith A. The phenomena of rupture and flow in solids. *Philos Trans R Soc Lond A*. 1921;221:163-198.
2. Williams ML. On the stress distribution at the base of a stationary crack. *J Appl Mech*. 1957;24(1):109-114.
3. Hillerborg A, Modéer M, Petersson P. Analysis of crack formation and crack growth in concrete by means of fracture mechanics and finite elements. *Cem Concr Res*. 1976;6(6):773-781.
4. Dugdale DS. Yielding of steel sheets containing slits. *J Mech Phys Solids*. 1960;8(2):100-104.
5. Barenblatt G. The mathematical theory of equilibrium cracks in brittle fracture. *Adv Appl Mech*. 1962;7:55-129.
6. Tvergaard V, Hutchinson J. The relation between crack growth resistance and fracture process parameters in elastic-plastic solids. *J Mech Phys Solids*. 1992;40(6):1377-1397.
7. Camacho G, Ortiz M. Computational modelling of impact damage in brittle materials. *Int J Solids Struct*. 1996;33(20):2899-2938.
8. Lin G, Kim Y, Cornec A, Schwalbe K. Fracture toughness of a constrained metal layer. *Comput Mater Sci*. 1997;9(1):36-47.
9. Moes N, Dolbow J, Belytschko T. A finite element method for crack growth without remeshing. *Int J Numer Methods Eng*. 1999;46:131-150.
10. Daux C, Moes N, Dolbow J, Sukumar N, Belytschko T. Arbitrary branched and intersecting cracks with the eXtended Finite Element Method. *Int J Numer Methods Eng*. 2000;48:1741-1760.
11. Areias P, Belytschko T. Analysis of three dimensional crack initiation and propagation using the extended finite element method. *Int J Numer Methods Eng*. 2005;63:760-788.
12. Silling SA. Reformulation of elasticity theory for discontinuities and long-range forces. *J Mech Phys Solids*. 2000;48:175-209.
13. Xu J, Askari A, Weckner O, Silling S. Peridynamic analysis of impact damage in composite laminates. *J Aerosp Eng*. 2008;21:187-194.
14. Silling S, Askari A. Peridynamic Model for Fatigue Cracking. Sandia Technical Report SAND2014-18590. 2014.
15. Ha Y, Bobaru F. Studies of dynamic crack propagation and crack branching with peridynamics. *Int J Fract*. 2010;162:229-244.
16. Ha Y, Bobaru F. Characteristics of dynamic brittle fracture captured with peridynamics. *Eng Fract Mech*. 2011;78(6):1156-1168.
17. Madenci E, Colavito K, Phan N. Peridynamics for unguided crack growth prediction under mixed-mode loading. *Eng Fract Mech*. 2016;167:34-44.
18. Wang Y, Zhou X, Wang Y, Shou Y. A 3-D conjugated bond-pair-based peridynamic formulation for initiation and propagation of cracks in brittle solids. *Int J Solids Struct*. 2017;134:89-115.
19. Silling S, Littlewood D, Seleson P. Variable horizon in a peridynamic medium. *J Mech Mater Struct*. 2015;10:591-612.
20. Galvanetto U, Mudric T, Shojaei A, Zaccariotto M. An effective way to couple fem meshes and peridynamics grids for the solution of static equilibrium problems. *Mech Res Commun*. 2016;76:41-47.
21. Zaccariotto M, Mudric T, Tomasi D, Shojaei A, Galvanetto U. Coupling of FEM meshes with peridynamic grids. *Comput Methods Appl Mech Eng*. 2017;330:471-497.
22. Lubineau G, Azdoud Y, Han F, Rey C, Askari A. A morphing strategy to couple non-local to local continuum mechanics. *J Mech Phys Solids*. 2012;60:1088-1102.
23. Kilic B, Madenci E. Coupling of peridynamic theory and the finite element method. *J Mech Mater Struct*. 2010;5(5):707-733.
24. Oterkus E. *Peridynamic Theory for Modeling Three-Dimensional Damage Growth in Metallic and Composite Structures*. PhD thesis, The University of Arizona; 2010.
25. Sun W, Fish J. Superposition-based coupling of peridynamics and finite element method. *Comput Mech*. 2019;64(1):231-248.
26. Sun W, Fish J, Zhang G. Superposition of non-ordinary state-based peridynamics and finite element method for material failure simulations. *Meccanica*. 2020;55(4):681-699.
27. Pagani A, Carrera E. Coupling 3D peridynamics and high order 1D finite elements based on local elasticity for the linear static analysis of solid beams and thin-walled reinforced structures. *Int J Numer Methods Eng*. 2020;121.
28. Ni T, Zaccariotto M, Zhu Q, Galvanetto U. Static solution of crack propagation problems in peridynamics. *Comput Methods Appl Mech Eng*. 2019;346:126-151.
29. Shojaei A, Zaccariotto M, Galvanetto U. Coupling of 2D discretized peridynamics with a meshless method based on classical elasticity using switching of nodal behaviour. *Eng Comput*. 2017;34(5):1334-1366.
30. Silling S, Epton M, Weckner O, Xu J, Askari E. Peridynamic states and constitutive modeling. *J Elast*. 2007;88:151-184.
31. Lehoucq R, Silling S, Plimpton S, Parks M. Peridynamics with LAMMPS: a user guide; 2008.
32. Macek R, Silling S. Peridynamics via finite element analysis. *Finite Elem Anal Des*. 2007;43:1169-1178.
33. Carrera E, Cinefra M, Petrolo M, Zappino E. *Finite Element Analysis of Structures through Unified Formulation*. John Wiley & Sons; 2014.
34. Pagani A, Azzara R, Augello R, Carrera E. Stress states in highly flexible thin-walled composite structures by unified shell model. *AIAA J*. 2021;1-14.
35. Pagani A, Sanchez-Majano AR. Influence of fiber misalignments on buckling performance of variable stiffness composites using layerwise models and random fields. *Mech Adv Mater Struct*. 2020;1-16.
36. Carrera E, Petrolo M. Refined beam elements with only displacement variables and plate/shell capabilities. *Meccanica*. 2012;47(3):537-556. doi:10.1007/s11012‐011‐9466‐5
37. Silling S, Askari E. A meshfree method based on the peridynamic model of solid mechanics. *Comput Struct*. 2005;83:1526-1535.
38. Durand R, Silva F. Three-dimensional modeling of fracture in quasi-brittle materials using plasticity and cohesive finite elements. *Int J Fract*. 2021;228:1-26.
39. Bobaru F, Yang M, Frota Alves L, Silling S, Askari E, Xu J. Convergence, adaptive refinement, and scaling in 1D peridynamics. *Int J Numer Methods Eng*. 2009;77:852-877.
40. Brokenshire DR. *A Study of Torsion Fracture Tests*. PhD thesis, Cardiff University; 1995.

41. Jefferson A, Barr BIG, Bennett T, Hee SC. Three dimensional finite element simulation of fracture test using craft concrete model. *Comput Concr*. 2004;1(3):261-284.
42. Gasser T, Holzapfel G. 3D crack propagation in unreinforced concrete: a two-step algorithm for tracking 3D crack paths. *Comput Methods Appl Mech Eng*. 2006;195:5198-5219.
43. Gurses E, Miehe C. A computational framework of three dimensional configurational-force-driven crack propagation. *Comput Methods Appl Mech Eng*. 2009;198:1413-1428.
44. Zreid I, Kaliske M. A gradient enhanced plasticity-damage microplane model for concrete. *Comput Mech*. 2018;62(5):1239-1257.
45. Ni T, Zaccariotto M, Zhu Q, Galvanetto U. Coupling of FEM and ordinary state-based peridynamics for brittle failure analysis in 3D. *Mech Adv Mater Struct*. 2019;28(9):875-890.

How to cite this article: Pagani A, Enea M, Carrera E. Quasi-static fracture analysis by coupled three-dimensional peridynamics and high order one-dimensional finite elements based on local elasticity. *Int J Numer Methods Eng*. 2022;123(4):1098-1113. doi: 10.1002/nme.6890